metals

MDPI

Article

Theoretical Study on Thermoelectric Properties and Doping Regulation of Mg_3X_2 (X = As, Sb, Bi)

Xiaofang Wang, Yong Lu, Ziyu Hu and Xiaohong Shao *

College of Mathematics and Physics, Beijing University of Chemical Technology, Beijing 100029, China; 2018200914@mail.buct.edu.cn (X.W.); luy@mail.buct.edu.cn (Y.L.); huziyu@mail.buct.edu.cn (Z.H.)
* Correspondence: shaoxh@mail.buct.edu.cn

Abstract: For searching both high-performances and better fits for near-room temperature thermoelectric materials, we here carried out a theoretical study on thermoelectric properties and doping regulation of Mg_3X_2 (X = As, Sb, Bi) by the combined method of first principle calculations and semi-classical Boltzmann theory. The thermoelectric properties of *n*-type Mg_3As_2, Mg_3Sb_2, and Mg_3Bi_2 were studied, and it was found that the dimensionless figures of merit, zT, are 2.58, 1.38, 0.34, and the *p*-type ones are 1.39, 0.64, 0.32, respectively. Furthermore, we calculated the lattice thermal conductivity of doped structures and screened out the structures with a relatively low formation energy to study the phonon dispersion and thermal conductivity in Mg_3X_2 (X = As, Sb, Bi). Finally, high thermoelectric zT and ultralow thermal conductivity of these doped structures was discussed.

Keywords: thermoelectric properties; doping; first principles calculation; Boltzmann theory

Citation: Wang, X.; Lu, Y.; Hu, Z.; Shao, X. Theoretical Study on Thermoelectric Properties and Doping Regulation of Mg_3X_2 (X = As, Sb, Bi). *Metals* **2021**, *11*, 971. https://doi.org/10.3390/met11060971

Academic Editor: Frank Czerwinski

Received: 21 May 2021
Accepted: 14 June 2021
Published: 17 June 2021

1. Introduction

Thermoelectric (TE) materials are non-polluted and can directly convert heat energy and electric energy to each other, and have a wide range of applications in areas such as waste heat recovery for power generation, car manufacturing and space probes. TE materials attract much attention. The TE efficiency can be measured by the dimensionless figure of merit, $zT = \frac{S^2\sigma T}{\kappa_e+\kappa_l}$, where S is the Seebeck coefficient, σ is the electrical conductivity, T is the absolute temperature, κ_e and κ_l are the electrical and lattice thermal conductivity, respectively. Power factor (*PF*) can be defined as the product of the square of Seebeck coefficient and the electrical conductivity, that is, $PF = S^2\sigma$. Therefore, it is essential to achieve a high power factor and a low thermal conductivity for a high zT value. As a result, discovering TE materials with outstanding properties is of great practical significance for many applications. Recently, many thermoelectric materials have been explored for power generation applications, such as GeTe [1], PbTe [2], half-Heusler [3] and skutterudites [4]. Among the reported TE materials, the Zintl phase, a class of intermetallic compounds, has been paid attention to because they meet the character of phonon-glass electron-crystal (PGEC) [5]. As the typical Zintl phase, Mg_3Sb_2 have been investigated experimentally and theoretically. Condron et al. [6] prepared Mg_3Sb_2 by a direct reaction of the elements and obtained the maximum zT value of 0.21 at 873 K. Chen et al. [7] got the maximum zT value ~0.6 at 773 K in $Mg_{2.975}Li_{0.025}Sb_2$ (*p*-type Li-doped Mg_3Sb_2). Wang et al. [8] carried out *p*-type Li-doping on Mg_3Sb_2 and got a higher zT value of 0.59 at 723 K. Xu et al. [9] explored theoretically the relation between the electronic structure and the TE properties of Mg_3Sb_2. Meng et al. [10] studied anisotropic thermoelectric in Mg_3Sb_2 and confirmed anisotropic thermoelectric of *p*-type Mg_3Sb_2. The low thermoelectric properties of thermoelectric materials limit their further application under a medium–low temperature; even when the ultralow thermal conductivity in MgSb-based materials was reported, the search for high thermoelectric materials and great potential as candidates for near-room temperature thermoelectric generators seems still to be more urgent. As and Bi belongs to the same main V group as Sb, by contrast, few studies are conducted on Mg_3Bi_2 and Mg_3As_2.

In this study, we investigated the thermoelectric properties of *n*-type and *p*-type Mg_3X_2 (X = As, Sb, Bi) systematically using the combined method of the first principles calculations and the semi-classical Boltzmann theory. A higher peak *zT* of 2.58 was obtained. In addition, we discussed the *n*-type and *p*-type doping effect in Mg_3X_2 (X = As, Sb, Bi), and the calculated doping formation energy and phonon dispersion curves proved that the doped structures are dynamically stable.

2. Computational Details

In this study, the structure of Mg_3X_2 (X = As, Sb, Bi) was built in VESTA (version 2.90.0b, Tohoku University, Sendai, Japan). The structure relaxations, the total density of states, projected density of states, and band structure were carried out in Vienna Ab-initio Simulation Package (VASP, vasp. 5.3.5.neb, University of Vienna, Vienna, Austria) based on density functional theory (DFT). The exchange-correlation functionals was described by the generalized gradient approximation (GGA) with Perdew, Burke, and Ernzerhof (PBE) functional [11]. The plane-wave cutoff energy was set to 400 eV and the energy convergence criterion was set up to 10^{-5} eV. The ionic relaxation was interrupted at -0.02 eV and was calculated by using $9 \times 9 \times 6$ Monkhorst-Pack grid meshes in irreducible Brillouin Zone. To get the phonon dispersion curves of these structures, the primitive cell of Mg_3X_2 (X = As, Sb, Bi) was expanded to a $3 \times 3 \times 2$ supercell in Phonopy package (version 1.9.6.1, National Institute for Material Science, Tsukuba, Japan) by the density functional perturbation theory (DFPT) [12]. The calculation of the TE transportation properties was based on the semi-classical Boltzmann theory and the rigid-band approach in the BoltzTrap code [13]. To verify the feasibility of doping on Mg_3X_2 (X = As, Sb, Bi), the formation energy of the doped structure was calculated using a $3 \times 3 \times 2$ supercell of Mg_3X_2 (X = As, Sb, Bi). We replaced one Mg atom with one Hf (Sn, Zr) atom for *n*-type doping, and with one Ag (Li, Na) atom for *p*-type doping, respectively. The doping concentration was 5.56%. The phonon dispersion curves, the total density of states, and projected density of states were calculated, where the K-Points were set as $3 \times 3 \times 3$.

3. Results and Discussion

3.1. Atomic and Electronic Structure

Figure 1 shows the structure of Mg_3X_2 (X = As, Sb, Bi). As is shown, the structure of Mg_3X_2 (X = As, Sb, Bi) belongs to the hexagonal system with the space group P-3m1 [14,15]. The relaxed lattice constants of them are shown in Table 1. The parameter we obtained was not more than 1.5% higher than that of the previous study and the parameter c we got was not more than 0.6% higher than that of the early research, which agrees with those in the previous study [16–18].

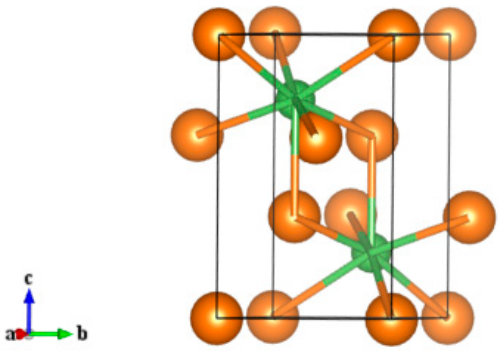

Figure 1. The crystal structure of Mg_3X_2 (X = As, Sb, Bi). Brown spheres represent the Mg atom, and the green spheres represent the X (As, Sb, Bi) atom.

Table 1. The structure parameters of Mg_3X_2 (X = As, Sb, Bi).

	a(Å)	c(Å)	Bond angle
Mg_3As_2	4.293 (4.264 [16])	6.763 (6.738 [16])	α = β = 90°, β = 120°
Mg_3Sb_2	4.596 (4.53 [17])	7.280 (7.24 [17])	α = β = 90°, β = 120°
Mg_3Bi_2	4.723 (4.67 [18])	7.44 (7.40 [18])	α = β = 90°, β = 120°

The band structures, total density of states (TDOS), and the projected density of states (PDOS) of Mg_3X_2 (X = As, Sb, Bi) are calculated and displayed from left to right in Figure 2. From the figure of the band structures, it can be seen that Mg_3Bi_2 may be a semimetal, which is consistent with the published researches [18,19]. Besides, Ferrier et al. [20,21] speculated that Mg_3Bi_2 is a semimetal on the basis of the conductivity-composition result they obtained, whereas Mg_3As_2 and Mg_3Sb_2 are both semiconductors. Mg_3As_2 has a direct band gap of 0.863 eV, and Mg_3Sb_2 has an indirect band gap of 0.205 eV, which is close to the band gap of 0.303eV of Mg_3Sb_2 by Yu et al. [22] by a different interactive correlation function in PW91. Obviously, it is seen from the figure of TDOS and PDOS that Mg *s*-orbital plays a major role in the total density of states at the conduction band minimum (CBM) of Mg_3As_2 and Mg_3Sb_2, while the peak of TDOS is mainly contributed by As *p*-orbital in Mg_3As_2 and Sb *p*-orbital in Mg_3Sb_2 at the valence band maximum (VBM), respectively. In Mg_3Bi_2, the TDOS at CBM was mainly controlled by the hybrid orbital of Mg *s*-orbital and Bi *p*-orbital, while Bi *p*-orbital contributes mainly at VBM.

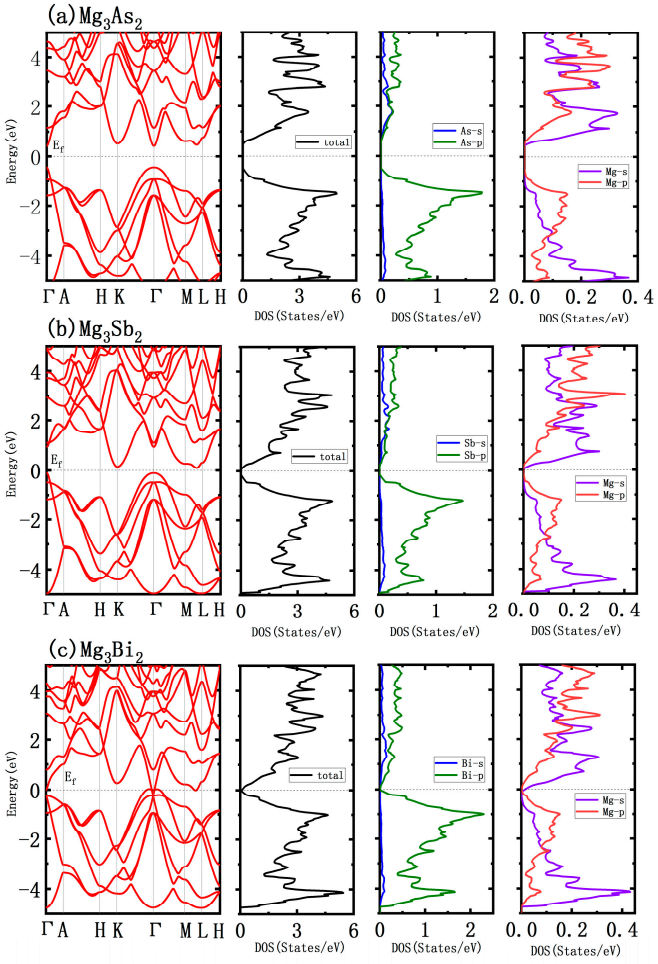

Figure 2. Band structures, TDOS (total density of states) and PDOS (projected density of states) of Mg_3X_2 (X = As, Sb, Bi). (**a**) Mg_3As_2, (**b**) Mg_3Sb_2, (c) Mg_3Bi_2. The symbols Γ, A, H, K, M, L in x-axis are high symmetry points. DOS means density of states.

3.2. Dynamics Stability

Figure 3a,c,e are the phonon dispersion curves and Figure 3b,d,f are the phonon density of states. Clearly, there are no imaginary frequencies in the three phonon dispersion curves, demonstrating that the three structures are all dynamically stable. The mixing of low frequency optical and acoustic modes demonstrates their strong phonon scattering, which benefits low lattice thermal conductivity.

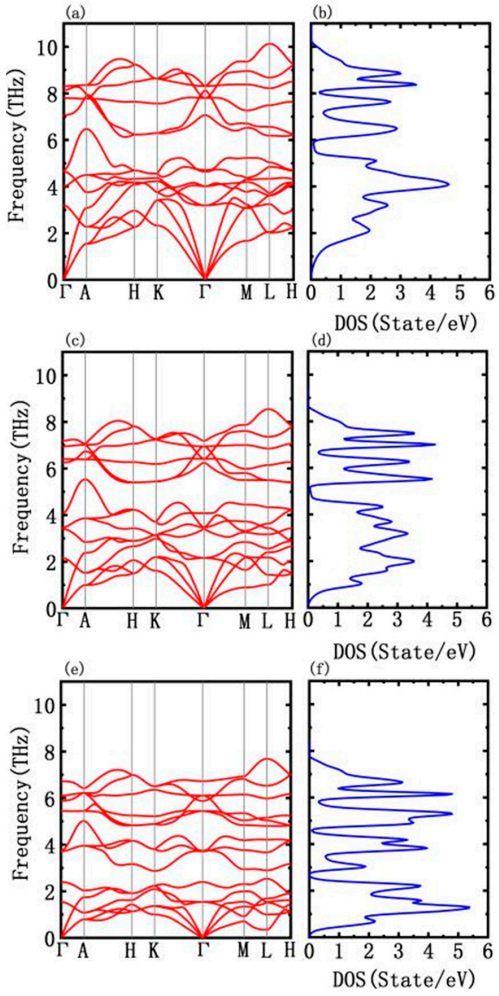

Figure 3. Phonon dispersion curves and phonon density of states of Mg_3X_2 (X = As, Sb, Bi), (**a**,**b**) Mg_3As_2; (**c**,**d**) Mg_3Sb_2; (**e**,**f**) Mg_3Bi_2.

The vibration of atoms at their equilibrium position can be described in as Debye temperature, which can be defined as, $\Theta_D = \frac{h}{k_B}\left(\frac{3n}{4\pi\Omega}\right)^{\frac{1}{3}} \nu_m$, in which h *is* Plank's constant, k_B is Boltzmann constant, n is the number of the unit cell, Ω is the volume of the unit cell, v_m is the average velocity of sound. Then v_m can be described by the transverse velocity of sound (v_t) and the longitudinal velocity of sound (v_l), the expression is as $v_m = \left[\frac{1}{3}\left(\frac{2}{v_t{}^3} + \frac{1}{v_l{}^3}\right)\right]^{-\frac{1}{3}}$, $v_t = \sqrt{\frac{G}{\rho}}$, $v_l = \sqrt{\frac{\left(B+\frac{4}{3}\,G\right)}{\rho}}$, where ρ is the density of materials, B and G are volume modulus and shear modulus. The elastic constants of c_{11}, c_{33}, c_{44}, c_{12}, c_{13} and B, G are calculated [14] of Mg_3As_2, Mg_3Sb_2, Mg_3Bi_2, respectively. According to the Debye theory, when the temperature is higher than the Debye temperature, the lattice thermal conductivity is proportional to 1/T, which can be approximately equal to the minimum lattice thermal conductivity. The minimum lattice thermal conductivity is calculated by $\kappa_{min} = \frac{1}{2}\left(\frac{\pi}{6}\right)^{\frac{1}{3}} k_B V^{-\frac{2}{3}} \left(2\nu_t + \nu_l\right)$, where V is the average volume of every atom in the unit cell. All the above results are shown in Table 2. The elastic constants we

calculated meet the Born stability criterion [23], demonstrating that the results are credible. The Debye temperature of Mg_3As_2, Mg_3Sb_2 and Mg_3Bi_2 is 332 K, 237 K and 175 K.

Table 2. Calculated elastic constants (c_{ij}), bulk modulus (B), shear modulus (G), density (ρ), volume (V), the transverse velocity of sound (v_t) and the longitudinal velocity of sound (v_l), the average velocity of sound (v_m), Debye temperature (Θ_D) and the minimum lattice thermal conductivity (κ_{min}).

	Mg_3As_2	Mg_3Sb_2	Mg_3Bi_2
c_{11} (GPa)	96.63	71.73	58.77
c_{33} (GPa)	90.89	75.91	65.52
c_{44} (GPa)	23.71	13.79	12.48
c_{12} (GPa)	45.84	36.78	32.06
c_{13} (GPa)	26.63	21.06	20.13
ρ (g/cm^3)	3.43	3.95	5.67
V (Å^3)	21.59	26.64	28.75
B (GPa)	53.28	41.83	36.39
G (GPa)	26.54	17.70	14.62
Θ_D (K)	332	237	175
v_t (m/s)	2782.50	2117.95	1605.26
v_l (m/s)	5085.97	4071.74	3138.67
v_m (m/s)	3102.70	2370.11	1798.33
κ_{min} (W/K)	0.76	0.52	0.38

3.3. Thermoelectric Transport Properties

Using the formula of $zT = \frac{S^2\sigma T}{\kappa_e+\kappa_l}$ and $\kappa_e = L\sigma T$, where L is the standard Lorenz number, $L = 2.45 \times 10^8 W\ \frac{\Omega}{K^2}$, we calculated the thermoelectric transport properties of Mg_3As_2, Mg_3Sb_2 and Mg_3Bi_2 by semi-classical Boltzmann theory and the rigid-band approach in the BoltzTrap code. Figure 4 presents the electrical conductivity of the n-type and p-type Mg_3X_2 (X = As, Sb, Bi). The carrier concentration of Mg_3Sb_2 is adopted as 1.47×10^{19} cm^{-3} from the experimental data at room temperature [24], and the electrical resistivity of p-type Ag-doped $Mg_{2.995}Ag_{0.005}Sb_2$ is about 8 mΩ cm. Based on the data of the experiment and the calculated result, the relaxation time of $\tau = 1.398 \times 10^{-14}$ s is obtained. Due to the lack of experimental data of Mg_3As_2 and Mg_3Bi_2, the same relaxation time as that of Mg_3Sb_2 is adopted. At the same time, σ can be defined as, $\sigma = ne\mu$, where n, e and μ are the carrier concentrations, the charge of an electron and the carrier mobility, respectively. As shown in Figure 4, the σ of n-type materials increases with the carrier concentration, whereas the σ of p-type ones have the same change trend.

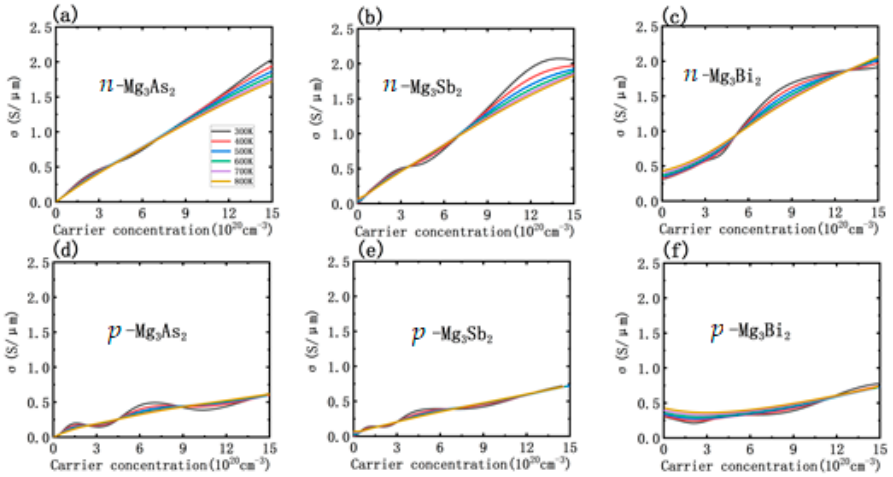

Figure 4. The electrical conductivity of the n-type and the p-type Mg_3X_2 (X = As, Sb, Bi) with carrier concentration. (**a**) n-Mg_3As_2, (**b**) n-Mg_3Sb_2, (**c**) n-Mg_3Bi_2, (**d**) p-Mg_3As_2, (**e**) p-Mg_3Sb_2, (**f**) p-Mg_3Bi_2.

Figure 5 is the electrical thermal conductivity of the *n*-type and *p*-type Mg_3X_2 (X = As, Sb, Bi) with carrier concentration. As can be seen, the electrical thermal conductivity increases with the temperature at the same carrier concentration for all the *n*-type or *p*-type Mg_3X_2 (X = As, Sb, Bi), and increases when the carrier concentration rises at the same temperature. It is noted that the electrical thermal conductivity value of *n*-type in the same material is generally larger than that of the *p*-type. Figure 6 displays the Seebeck coefficient of the *n*-type and *p*-type Mg_3X_2 (X = As, Sb, Bi). As shown, the *S* of *n*-type Mg_3X_2 (X = As, Sb, Bi) is negative, while that of most *p*-type material curves is positive. For Mg_3As_2 and *n*-type Mg_3Bi_2, the absolute value of *S* increases when the temperature increases. For Mg_3Sb_2 and *p*-type Mg_3Bi_2 at a low carrier concentration, the absolute value of the Seebeck coefficient decreases with the temperature increases, which is due to the influence of the bipolar effect. The bipolar effect usually occurs in wide band gap semiconductors at high temperatures and narrow band gap semiconductors at room temperature. With the higher carrier concentration, the absolute value of Mg_3Sb_2 and *p*-type Mg_3Bi_2' s *S* increases with the temperature increases.

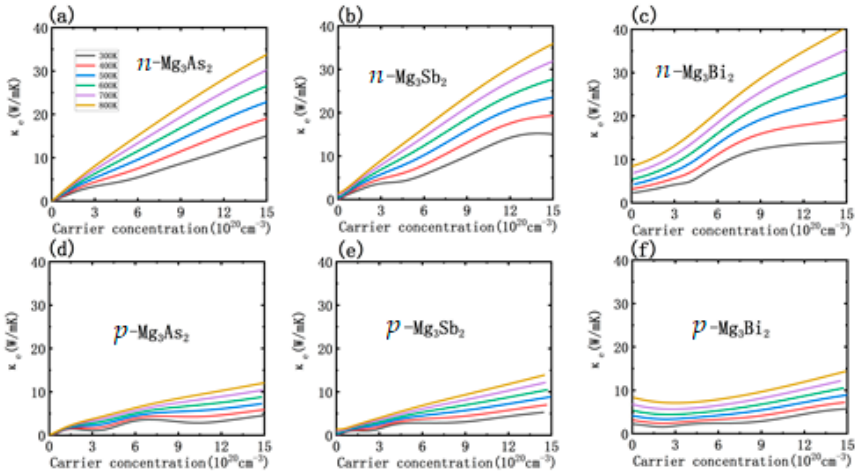

Figure 5. The electrical thermal conductivity of the *n*-type and the *p*-type Mg_3X_2 (X = As, Sb, Bi) with carrier concentration. (**a**) *n*-Mg_3As_2, (**b**) *n*-Mg_3Sb_2, (**c**) *n*-Mg_3Bi_2, (**d**) *p*-Mg_3As_2, (**e**) *p*-Mg_3Sb_2, (**f**) *p*-Mg_3Bi_2.

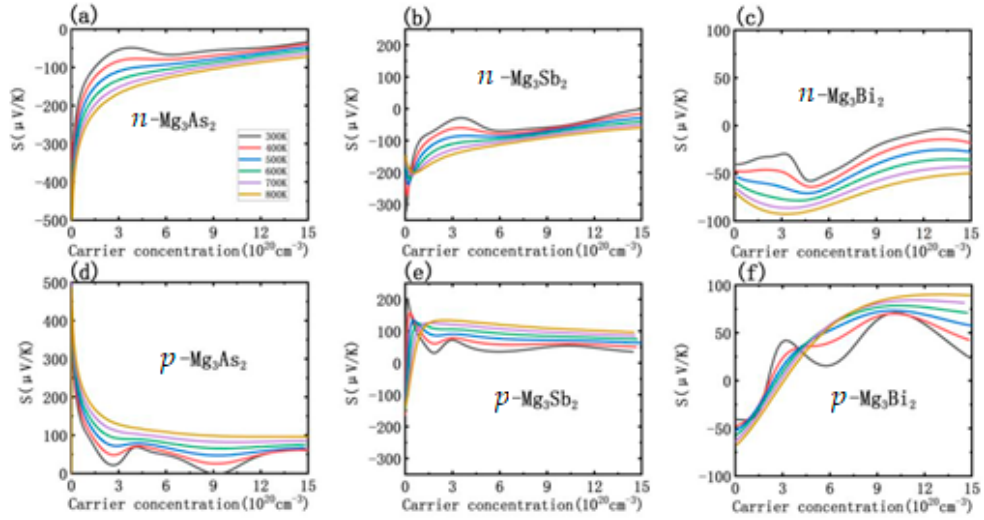

Figure 6. The Seebeck coefficient of the *n*-type and the *p*-type Mg_3X_2 (X = As, Sb, Bi) with carrier concentration. (**a**) *n*-Mg_3As_2, (**b**) *n*-Mg_3Sb_2, (**c**) *n*-Mg_3Bi_2, (**d**) *p*-Mg_3As_2, (**e**) *p*-Mg_3Sb_2, (**f**) *p*-Mg_3Bi_2.

Figure 7 is the power factor performance with the carrier concentration of the *n*-type and *p*-type Mg_3X_2 (X = As, Sb, Bi). For *n*-type one, PF increases first and then decreases when the carrier concentration increases. In addition, it can be found that, with the same carrier concentration, the power factor of *n*-type material and *p*-type Mg_3As_2 increases with the temperature gradually. However, it is an exception to that of *p*-type Mg_3Sb_2 and *p*-type Mg_3Bi_2 at a low concentration due to the influence of the negative Seebeck coefficient.

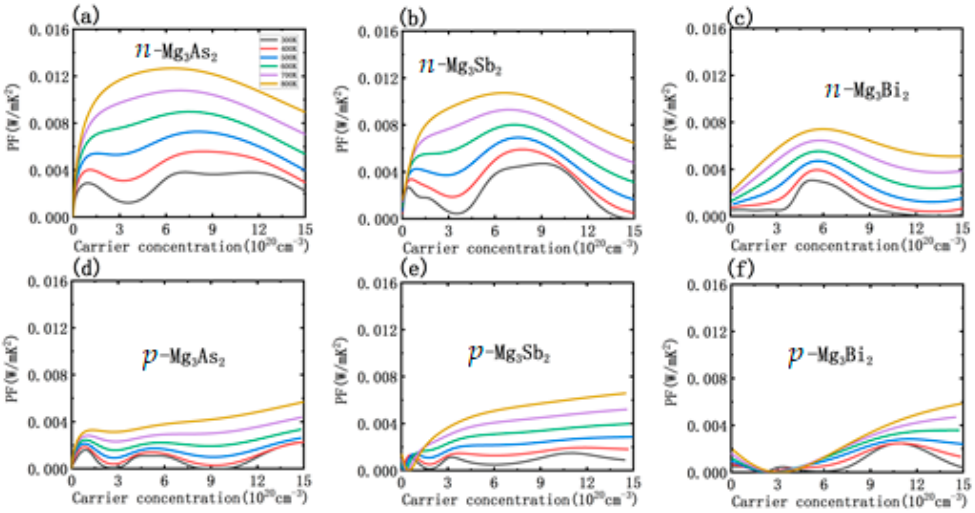

Figure 7. The power factor of the *n*-type and the *p*-type Mg_3X_2 (X = As, Sb, Bi) with carrier concentration. (**a**) *n*-Mg_3As_2, (**b**) *n*-Mg_3Sb_2, (**c**) *n*-Mg_3Bi_2, (**d**) *p*-Mg_3As_2, (**e**) *p*-Mg_3Sb_2, (**f**) *p*-Mg_3Bi_2.

Figure 8 demonstrates the *zT* values of the *n*-type and *p*-type Mg_3X_2 (X = As, Sb, Bi). The *zT* increases with temperature ranging from 300 K to 800 K. The *n*-type and *p*-type Mg_3Bi_2 have the maximum *zT* values of 0.34 and 0.32, respectively, and that of the *n*-type and *p*-type Mg_3Sb_2 can reach 1.38 and 0.64, respectively. It is noted that the maximum *zT* value of *n*-type and *p*-type Mg_3As_2 can achieve 2.58 and 1.39, which is competitive among most published results, indicating that Mg_3As_2 is a promising candidate for TE materials.

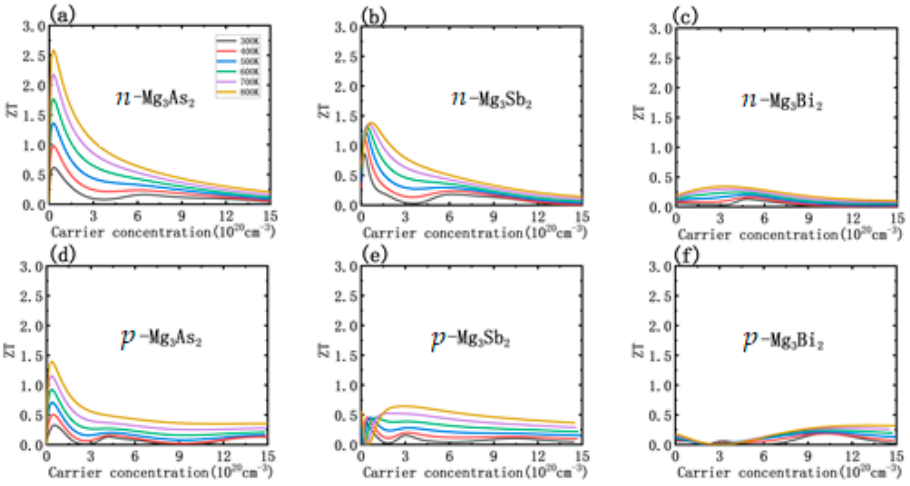

Figure 8. The *zT* values of the *n*-type and the *p*-type Mg_3X_2 (X = As, Sb, Bi) with carrier concentration. (**a**) *n*-Mg_3As_2, (**b**) *n*-Mg_3Sb_2, (**c**) *n*-Mg_3Bi_2, (**d**) *p*-Mg_3As_2, (**e**) *p*-Mg_3Sb_2, (**f**) *p*-Mg_3Bi_2.

3.4. Doping Effect

The studies above show that Mg_3X_2 (X = As, Sb, Bi) have good TE properties and potential application prospects. The doping strategy is considered as an effective approach for improving TE performance; therefore, further investigations into doping were carried

out in this work. To verify the feasibility of doping on Mg_3X_2 (X = As, Sb, Bi), elements of Hf (or Sn, Zr, Ag, Li and Na) atom substituting to the Mg atom are investigated. The formation energy of each doped structure is calculated by $E_f = E(Mg_{53}YX_{36}) - E(Mg_{54}X_{36}) - E(Y) + E(Mg)$, where X can be As, Sb or Bi. Y can be Hf, Sn, Zr, Ag, Li and Na. The results are shown in Table 3. The formation energies of $Mg_{53}ZrAs_{36}$, $Mg_{53}ZrSb_{36}$, $Mg_{53}ZrBi_{36}$ and $Mg_{53}SnBi_{36}$ are relatively lower of *n*-type doping, while those of $Mg_{53}LiAs_{36}$, $Mg_{53}LiSb_{36}$, $Mg_{53}NaSb_{36}$, $Mg_{53}LiBi_{36}$ and $Mg_{53}NaBi_{36}$ are relatively lower of *p*-type doping, wherein the negative formation energy indicates the stability of the structure. The phonon dispersion curves are calculated (shown in Figure 9) and the corresponding density of states are shown in Figure 10. Figure 9 presents that all doped structures have no imaginary frequencies, indicating that all the doped structures are dynamically stable. Compared with the phonon dispersion curve of the un-doped structure, the slope of the acoustic mode of the doped one decreases, which proves that the doped structure has a lower phonon group velocity. The mixing amplitude of the low-frequency optical mode and the acoustic one increases, demonstrating the strong phonon scattering between them, especially in the doped $Mg_{54}Bi_{36}$. Figure 10 reveals TDOS and PDOS of the doped structures. The doping of an atom does not affect the dominant contribution orbitals to the density of states, but the band gaps move to the lower energy direction for *n*-type doped systems, while moving to the higher energy direction for *p*-type doped ones. In addition, we calculated the lattice thermal conductivity of doped structures shown in Table 4. As is shown, the lattice thermal conductivity and Debye temperature was reduced by doping except $Mg_{53}ZrBi_{36}$ and $Mg_{53}SnBi_{36}$. Therefore, it can be safely concluded that implementing *n*-type and *p*-type doping on Mg_3X_2 (X = As, Sb, Bi) by replacing an Mg atom can improve the thermoelectric properties.

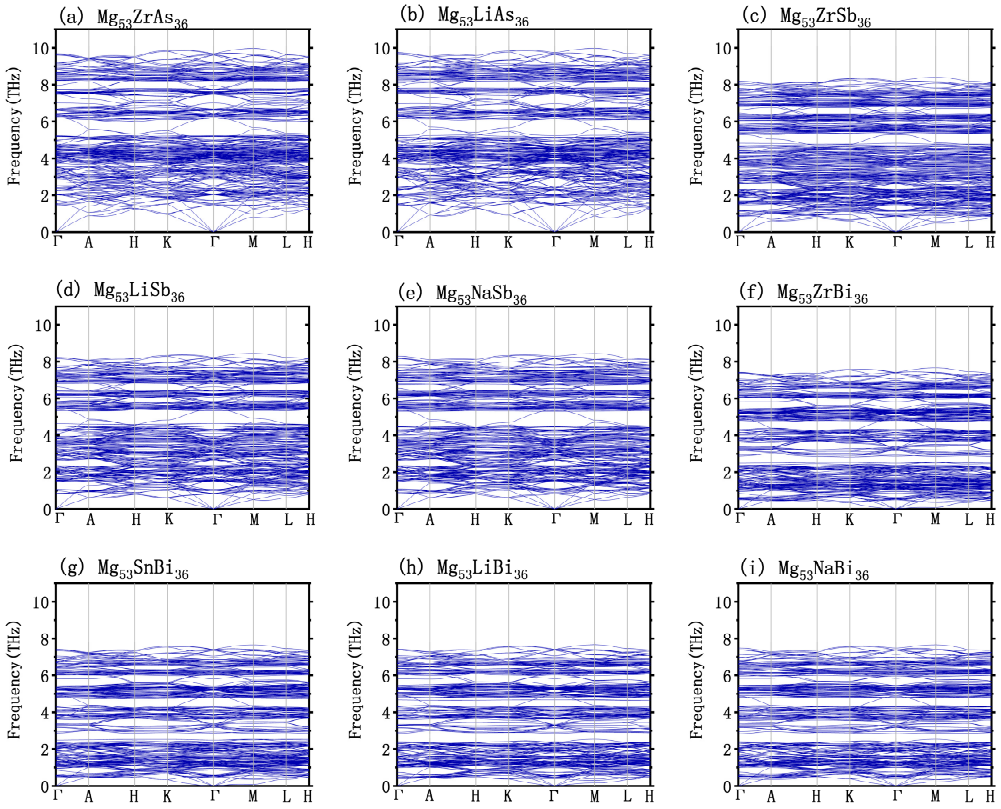

Figure 9. Phonon dispersion curves of doped 3 × 3 × 2 Mg_3X_2 (X = As, Sb, Bi). (**a**) $Mg_{53}ZrAs_{36}$, (**b**) $Mg_{53}LiAs_{36}$, (**c**) $Mg_{53}ZrSb_{36}$, (**d**) $Mg_{53}LiSb_{36}$, (**e**) $Mg_{53}NaSb_{36}$, (**f**) $Mg_{53}ZrBi_{36}$, (**g**) $Mg_{53}SnBi_{36}$, (**h**) $Mg_{53}LiBi_{36}$, (**i**) $Mg_{53}NaBi_{36}$.

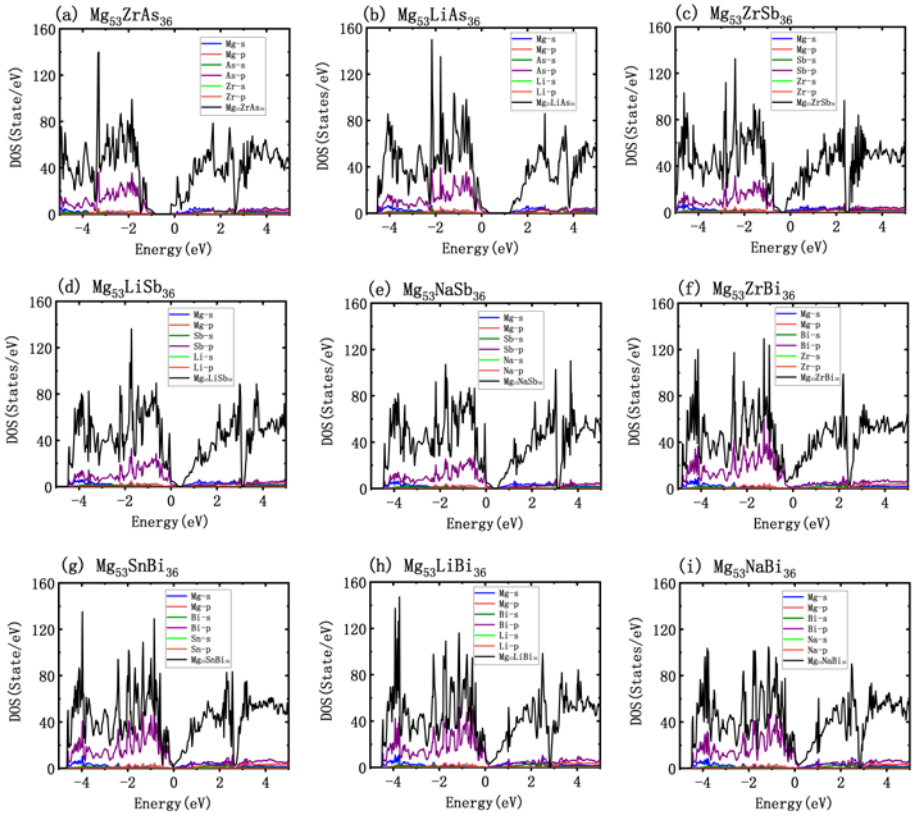

Figure 10. TDOS and PDOS of doped 3 × 3 × 2 Mg_3X_2 (X = As, Sb, Bi). (**a**) $Mg_{53}ZrAs_{36}$, (**b**) $Mg_{53}LiAs_{36}$, (**c**) $Mg_{53}ZrSb_{36}$, (**d**) $Mg_{53}LiSb_{36}$, (**e**) $Mg_{53}NaSb_{36}$, (**f**) $Mg_{53}ZrBi_{36}$, (**g**) $Mg_{53}SnBi_{36}$, (**h**) $Mg_{53}LiBi_{36}$, (**i**) $Mg_{53}NaBi_{36}$.

Table 3. The formation energy (E_f) of *n*-type (Hf, Sn, Zr) and *p*-type (Ag, Li, Na) doping on 3 × 3 × 2 supercell of Mg_3X_2 (X = As, Sb, Bi).

	E_f ($Mg_{53}YAs_{36}$)	E_f ($Mg_{53}YSb_{36}$)	E_f ($Mg_{53}YBi_{36}$)
Y = Hf (n)	0.97	2.41	0.98
Y = Sn (n)	1.22	2.62	0.50
Y = Zr (n)	0.55	2.09	0.50
Y = Ag (p)	1.89	1.32	1.05
Y = Li (p)	0.26	−0.14	−0.35
Y = Na (p)	0.36	−0.14	−0.39

Table 4. Calculated transverse velocity of sound (v_t) and longitudinal velocity of sound (v_l), Debye temperature (Θ_D) and the minimum lattice thermal conductivity (κ_{min}) of doped 3 × 3 × 2 Mg_3X_2 (X = As, Sb, Bi).

	v_l (m/s)	v_t (m/s)	Θ_D (K)	κ_{min} (W/mK)
Mg_3As_2	5085.97	2782.52	332	0.76
$Mg_{53}ZrAs_{36}$ (*n*)	5036.81	2735.55	326	0.75
$Mg_{53}LiAs_{36}$ (*p*)	4841.40	2462.41	295	0.70
Mg_3Sb_2	4071.74	2117.95	237	0.52
$Mg_{53}ZrSb_{36}$ (*n*)	3998.69	2051.21	229	0.50
$Mg_{53}LiSb_{36}$ (*p*)	4014.01	2051.68	229	0.51
$Mg_{53}NaSb_{36}$ (*p*)	4009.55	2045.79	228	0.50
Mg_3Bi_2	3138.67	1605.26	175	0.38
$Mg_{53}ZrBi_{36}$ (*n*)	3134.87	1613.38	176	0.38
$Mg_{53}SnBi_{36}$ (*n*)	3149.64	1608.67	175	0.38
$Mg_{53}LiBi_{36}$ (*p*)	3053.87	1503.96	164	0.36
$Mg_{53}NaBi_{36}$ (*p*)	3050.20	1493.58	163	0.36

4. Conclusions

In summary, the thermoelectric properties of Mg_3X_2 (X = As, Sb, Bi) were studied by first principles and semi-classical Boltzmann theory. The calculated results show that the maximum zT values of n-type Mg_3Sb_2 and p-type Mg_3Sb_2 are 1.38 and 0.64, respectively. The maximum zT values of n-type Mg_3Bi_2 and p-type Mg_3Bi_2 are 0.34 and 0.32 respectively, and these maximum values were obtained at a temperature of 800 K. It is noted that Mg_3As_2 is a direct bandgap semiconductor with a band gap of 0.8626 eV, and the maximum zT of n-type and p-type Mg_3As_2 can reach 2.58 and 1.39, respectively. Based on the calculation results, the element of Hf (or Sn, Zr, Ag, Li and Na) substituting to Mg atoms in doped Mg_3X_2 (X = As, Sb, Bi) is investigated, and the formation energy and stability of the p-type doping of Li for Mg_3As_2, p-type doping of Li and Na for Mg_3Sb_2, and p-type doping of Li and Na for Mg_3Bi_2 was discussed.

Author Contributions: Conceptualization, X.S., Y.L. and X.W.; methodology, Y.L. and X.W.; formal analysis, X.W.; writing—original draft preparation, X.W.; writing—review and editing, X.S. and Z.H. All authors have read and agreed to the published version of the manuscript.

Funding: This work was supported by the National Natural Science Foundation of China (Grant No.11604008 and 12074028).

Institutional Review Board Statement: Not applicable.

Informed Consent Statement: Not applicable.

Data Availability Statement: Data sharing is not applicable to this article.

Conflicts of Interest: The authors declare no conflict of interest.

References

1. Gelbstein, Y.; Davidow, J.; Leshem, E.; Pinshow, O.; Moisa, S. Significant lattice thermal conductivity reduction following phase separation of the highly efficient $Ge_xPb_{1-x}Te$ thermoelectric alloys. *Phys. Status Solidi B* **2014**, *251*, 1431–1437. [CrossRef]
2. Ben-Ayoun, D.; Sadia, Y.; Gelbstein, Y. High temperature thermoelectric properties evolution of $Pb_{1-x}Sn_xTe$ based alloys. *J. Alloys Compd.* **2017**, *722*, 33–38. [CrossRef]
3. Xing, Y.; Liu, R.; Liao, J.; Zhang, Q.; Xia, X.; Wang, C.; Huang, H.; Chu, J.; Gu, M.; Zhu, T.; et al. High-efficiency half-Heusler thermoelectric modules enabled by self-propagating synthesis and topologic structure optimization. *Energy Environ. Sci.* **2019**, *12*, 3390. [CrossRef]
4. Rull-Bravo, M.; Moure, A.; Fernández, J.F.; Martín-González, M. Skutterudites as thermoelectric materials: Revisited. *RSC Adv.* **2015**, *5*, 41653–41667. [CrossRef]
5. Kauzlarich, S.M.; Brown, S.R.; Snyder, G.J. Zintl phases for thermoelectric devices. *Dalton Trans.* **2007**, *21*, 2099–2107. [CrossRef]
6. Condron, C.L.; Kauzlarich, S.M.; Gascoin, F.; Snyder, G.J. Thermoelectric Properties and Microstructure of Mg_3Sb_2. *J. Solid State Chem.* **2016**, *179*, 2252–2257. [CrossRef]
7. Chen, C.; Li, X.; Li, S.; Wang, X.; Zhang, Z.; Sui, J.; Cao, F.; Liu, X.; Zhang, Q. Enhanced thermoelectric performance of p-type Mg_3Sb_2 by lithium doping and its tunability in an anionic framework. *J. Mater. Sci.* **2018**, *53*, 16001–16009. [CrossRef]
8. Wang, H.; Chen, J.; Lu, T.; Zhu, K.; Li, S.; Liu, J.; Zhao, H. Enhanced thermoelectric performance in p-type Mg_3Sb_2 via lithium doping. *Chin. Phys. B.* **2018**, *4*, 110–116.
9. Xu, B.; Rao, L.; Yu, G.; Ma, S.; Wang, Y.; Wang, Y.; Yi, L. The Relation between the Electronic Structure and Thermoelectric Properties for Zintl Compounds Mg_3Sb_2. *J. Phys. Soc. Jpn.* **2017**, *86*, 024601. [CrossRef]
10. Meng, F.; Sun, S.; Ma, J.; Chronister, C.; He, J.; Li, W. Anisotropic thermoelectric figure-of-merit in Mg_3Sb_2. *Mater. Today Phys.* **2020**, *13*, 100217. [CrossRef]
11. Perdew, J.; Burke, K.; Ernzerhof, M. Generalized gradient approximation made simple. *Phys. Rev. Lett.* **1996**, *77*, 3865–3868. [CrossRef]
12. Gonze, X.; Lee, C. Dynamical matrices, Born effective charges, dielectric permittivity tensors, and interatomic force constants from density-functional perturbation theory. *Phys. Rev. B Condens. Matter.* **1997**, *55*, 10355–10368. [CrossRef]
13. Madsen, G.; Singh, D.J. BoltzTraP. A code for calculating band-structure dependent quantities. *Comput. Phys. Commun.* **2006**, *175*, 67–71. [CrossRef]
14. Jun-ichi, T.; Takahashi, M.; Kido, H. Lattice dynamics and elastic properties of Mg_3As_2 and Mg_3Sb_2 compounds from first-principles calculations. *Phys. B Condens. Matter* **2010**, *405*, 4219–4225. [CrossRef]
15. Lee, J.; Monserrat, B.; Seymour, I.D.; Liu, Z.; Dutton, S.E.; Grey, C.P. An ab initio investigation on the electronic structure, defect energetics, and magnesium kinetics in Mg_3Bi_2. *J. Mater. Chem. A.* **2018**, *6*, 16983–16991. [CrossRef]

16. Juza, R.; Kroebel, R. Über eine Hochtemperaturmodifikation des Magnesiumarsenids und eine ternre Phase Mg_2MnAs_2 gleicher Struktur. *Z. Für Anorg. Allg. Chem.* **1964**, *331*, 187–199. [CrossRef]
17. Sevast'yanova, L.G.; Kravchenko, O.V.; Gulish, O.K.; Stupnikov, V.A.; Leonova, M.E.; Zhizhin, M.G. Binary and ternary compounds in the Mg-Sb-B and Mg-Bi-B systems as catalysts for the synthesis of cubic BN. *Inorg. Mater.* **2006**, *42*, 863–866. [CrossRef]
18. Imai, Y.; Watanabe, A. Electronic structures of Mg_3Pn_2 (Pn=N, P, As, Sb and Bi) and Ca_3N_2 calculated by a first-principle pseudopotential method. *J. Mater. Sci.* **2006**, *41*, 2435–2441. [CrossRef]
19. Xu, R.; Groot, R.; van der Lugt, W. Resistivities and band structures of alkaline-earth-pnictide systems. *J. Phys. Condens. Matter* **1993**, *5*, 7551–7562. [CrossRef]
20. Ferrier, R.P.; Herrell, D.J. Conduction in amorphous magnesium-bismuth alloys. *Philos. Mag. A J. Theor. Exp. Appl. Phys.* **1969**, *19*, 853–868. [CrossRef]
21. Ferrier, R.P.; Herrell, D.J. The structure and electrical properties of amorphous MgBi and MgSb alloys. *J. Non-Cryst. Solids* **1970**, *4*, 338–344. [CrossRef]
22. Yu, W.Y.; Tang, B.Y.; Peng, L.M.; Ding, W.J. Electronic structure and mechanical properties of α-Mg_3Sb_2. *Acta Phys. Sin.* **2009**, *58*, 216–223.
23. Wu, Z.J.; Zhao, E.J.; Xiang, H.P.; Hao, X.F.; Liu, X.J.; Meng, J. Crystal structures and elastic properties of superhard IrN_2 and IrN_3 from first principles. *Phys. Rev. B.* **2007**, *76*, 054115. [CrossRef]
24. Song, L.; Zhang, J.; Iversen, B.B. Simultaneous improvement of power factor and thermal conductivity via Ag doping in p-type Mg_3Sb_2 thermoelectric materials. *J. Mater. Chem. A.* **2017**, *5*, 4932–4939. [CrossRef]